# Chapter 11
# Functional Magnetic Resonance Imaging

**John A. Sexton, Gopikrishna Deshpande, Zhihao Li, Christopher B. Glielmi, and Xiaoping P. Hu**

## 1 Principles of MRI

Nuclear magnetic resonance, the physical phenomenon which makes MRI possible, occurs in atoms with an odd number of protons and/or an odd number of neutrons. The nuclei of such atoms possess a property known as spin angular momentum ($\vec{J}$) and an associated magnetic dipole moment ($\vec{\mu}$):

$$\vec{\mu} = \gamma \times \vec{J}, \tag{11.1}$$

where $\gamma$ is the nucleus-specific gyromagnetic ratio.[1] Nuclei with a magnetic dipole moment (called "spins") are subject to the effects of an externally applied magnetic field. The single-proton nucleus of the Hydrogen atom is most commonly used for MR imaging because it possesses a relatively large magnetic moment and is found in abundance throughout the human body (primarily in $H_2O$).

In the context of imaging it is convenient to consider the net magnetization ($\vec{M}$), or magnetic moment per unit volume, of many spins. In the absence of an external

[1] For hydrogen, $\gamma = 267.513$ radians per second per Tesla, or 42.576 MHz per Tesla.

J.A. Sexton • Z. Li • X.P. Hu (✉)
Coulter Department of Biomedical Engineering, Georgia Tech and Emory University, Atlanta, GA 30322, USA
e-mail: john.a.sexton@emory.edu; zli8@emory.edu; xhu@emory.edu

G. Deshpande
Department of Electrical and Computer Engineering, Auburn University, Auburn, AL 36849, USA
e-mail: gopi@auburn.edu

C.B. Glielmi
Siemens Healthcare, MR Research and Development, Chicago, IL 60611, USA
e-mail: christopher.glielmi@siemens.com

B. He (ed.), *Neural Engineering*, DOI 10.1007/978-1-4614-5227-0_11,

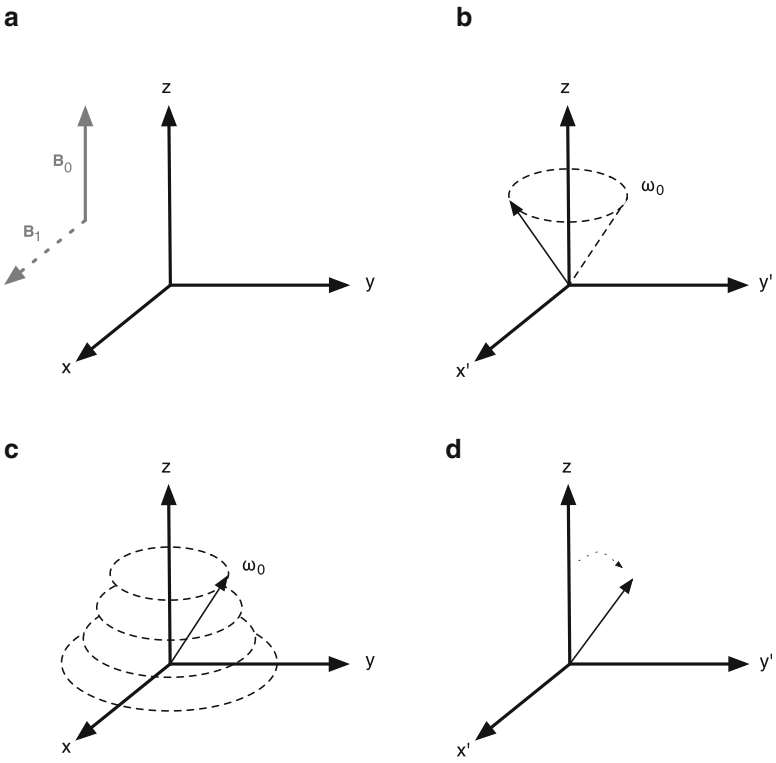


**Fig. 11.1** (**a**) The fixed laboratory frame and (**b**) the rotating frame of reference. $B_0$ is parallel to $z$ and $z'$ while the $x'$ and $y'$ axes rotate around the $z$ axis at $\omega_0$. The RF pulse $B_1$ is applied perpendicular to $B_0$ to tip $M$ into the transverse ($x$–$y$) plane. The motion of $M$ in the laboratory frame of reference (**c**) is complex compared to that in the rotating frame (**d**)

magnetic field, thermal activity and internal dipole fields leave the spins within a given volume oriented randomly and with zero net magnetization. In the presence of a magnetic field (known as the static field or $B_0$), about half of the spins will align parallel to the field, while about half of the spins will align antiparallel to it. A tiny majority of the spins[2] will align parallel to it, resulting in a nonzero net magnetization $\vec{M}$ aligned parallel to the field.

The angular momentum of spins which comprise $\vec{M}$ causes those spins, and hence $\vec{M}$ itself, to precess about the applied field $\vec{B}_0$ (see Fig. 11.1b). The frequency of this precession is given by the Larmor Equation:

$$\omega_0 = \gamma \times B_0. \tag{11.2}$$

[2] About five spins out per million at a field strength of 1.5 T. The difference in populations is small because the difference in energy levels between the parallel and antiparallel states is small.

The magnitude of the net magnetization $\vec{M}$ is very small compared to that of $B_0$; therefore when $\vec{M}$ is aligned parallel to $B_0$ it is difficult to measure. To detect the magnetization, it is tipped away from $B_0$ by a second magnetic field, known as the radio-frequency (RF) pulse or $B_1$, which is applied perpendicular to $B_0$. When the oscillation frequency of $B_1$ matches the Larmor frequency of spins in a target volume, the RF pulse is said to be "on resonance" with those spins. The RF Pulse is usually applied for a short duration ($t$), which causes $\vec{M}$ to rotate away from $B_0$ by a "flip angle" given by $\theta = \gamma B_1 t$.

When $B_1$ is applied, the magnetization will simultaneously precess about $B_0$ at frequency $\omega_0$ and about $B_1$ at frequency $\omega_1$. In a fixed frame of reference ($x$, $y$, $z$), the resulting motion of $\vec{M}$ is complicated (see Fig. 11.1c). It can be simplified by introducing a frame of reference ($x'$, $y'$, $z'$) which rotates about $B_0$ at the same frequency and direction as $\vec{M}$. Under these conditions, $\vec{M}$ appears stationary in the rotating frame when precessing about $B_0$ (Fig. 11.1d).

The rotation of $\vec{M}$ away from the direction of $B_0$ leads to a component of the net magnetization that is perpendicular to $B_0$. This component is known as the transverse magnetization and is the source of the signal measured with MRI. The component of $\vec{M}$ which remains parallel to $B_0$ is known as the longitudinal magnetization.

Once excited by $B_1$, spins tend to release the energy they absorbed in a process known as relaxation. There are two relaxation processes, characterized by relaxation times $T_1$ and $T_2$. $T_1$ is known as "spin–lattice" relaxation and characterizes the rate at which excited spins exchange energy with their surrounding environment. This time constant dictates how quickly the longitudinal magnetization returns back to its equilibrium value. $T_2$ is known as "spin–spin" relaxation and reflects the rate at which excited spins exchange energy with one another. This time constant describes the rate at which the transverse magnetization decays to zero. A third parameter $T_2^*$ accounts for the accelerated decay of the observed transverse magnetization in the presence of magnetic field inhomogeneities ($\Delta B$) and $T_2$ decay:

$$\frac{1}{T_2^*} = \frac{1}{T_2} + \gamma \times \Delta B. \tag{11.3}$$

According to Faraday's law, precessional motion of a net magnetization vector which has a transverse component will generate a time-varying magnetic flux through a nearby receiver coil. This flux in turn generates a voltage in the receiver coil which oscillates at the Larmor frequency of the spins which created it. This voltage is the measured NMR signal, which reflects the volume integral of the transverse magnetization over time.

Magnetic Resonance Imaging (MRI) aims to map the measured NMR signal (and therefore resonance frequency) to a specific location in space ($\vec{r}$). Since resonance frequency at a given point is determined by the strength of the local magnetic field, it is possible to control the distribution of resonance frequencies in space by causing the magnetic field to vary in a predictable way. This is achieved with the application of linear magnetic field gradients superimposed on top of $B_0$. This situation is illustrated for a gradient applied along the $x$-axis in Fig. 11.2.

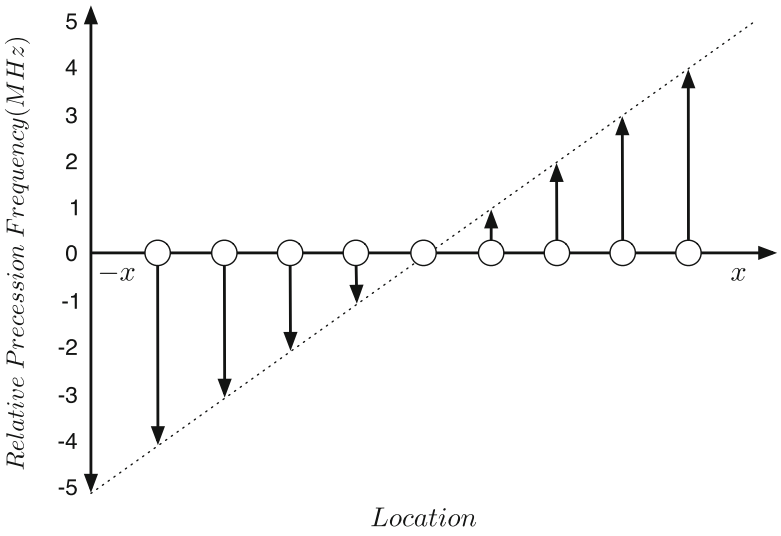


**Fig. 11.2** Gradient field localization of precession frequency along the $x$-axis. Gradient fields are imposed on top of $B_0$, causing precession frequency to vary with position. Larger arrows indicate larger precession frequencies

Most MRI experiments encode magnetization information from one slice of the volume of interest at a time. Slice selection is achieved by applying a radio-frequency pulse with bandwidth $\Delta\omega$ (centered on the resonance frequency of the target slice $\omega$) together with a linear field gradient in the slice-select direction (e.g., along the $z$-axis). This RF pulse excites spins within a slice of thickness $\Delta z$ whose Larmor frequencies fall within the frequency range of the RF pulse ($\Delta\omega$). Once excited, the task of image formation is then to distinguish signals from different locations in the slice of interest before the transverse magnetization decays away.

To create an image, the resonance frequencies of spins within an excited slice must be differentiated with additional magnetic field gradients. Generally such spins are encoded in terms of local frequency and phase.

Assuming the excited slice to be in the $xy$-plane, applying a linear gradient $G_x$ along the $x$ direction will cause the precession frequency of spins to vary according to their position along the $x$-axis (see Fig. 11.2).

If an additional gradient $G_y$ is applied along the $y$ direction for a short period $\tau_{pe}$ and then turned off, spins will accumulate phase relative to one another based on their position along the $y$-axis during the time interval $[0, \tau_{pe}]$ (see Fig. 11.3). For a slice centered at location $z_0$ with slice thickness $\Delta z$, the signal measured at location $\vec{\mathbf{r}}$ at time $t$ may then be written as follows:

$$S'(\vec{\mathbf{r}},\ t) = \int\int\int_{z_0-\frac{\Delta z}{2}}^{z_0+\frac{\Delta z}{2}} \rho_M(\vec{\mathbf{r}}) \mathrm{e}^{-\mathrm{i}\gamma\left(G_z \cdot z \cdot t + G_y \cdot y \cdot \tau_{\mathrm{pe}}\right)} \mathrm{d}x\ \mathrm{d}y\ \mathrm{d}z. \tag{11.4}$$

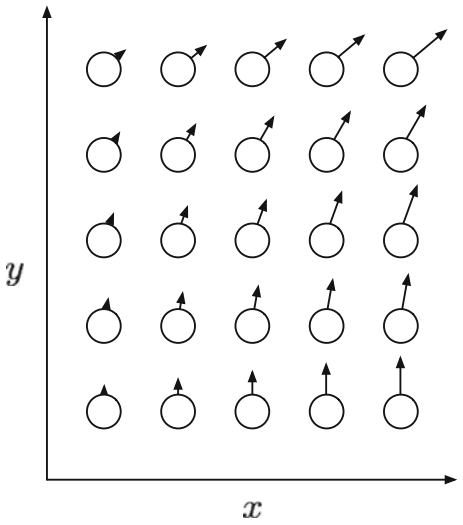


**Fig. 11.3** Frequency and phase encoding in two dimensions. Precession frequency increases from *left* to *right*, while phase increases from *bottom* to *top*. Each spin has a unique combination of frequency and phase which corresponds to its location in space

This equation is a 2D Fourier Transform between resonance frequency and location in space. Though resonance frequency is what MRI actually measures, investigators using MRI are generally interested in the spatial information—images of the body. Therefore an image may be reconstructed through an inverse 2-dimensional Fourier transform of the measured resonance frequencies.

Once spins in a given volume are excited, the signal they generate will decay according to the time constants T1 and T2 as described above. The type of signal most commonly measured in MRI is called an echo. To form an echo, the transverse magnetization is intentionally de-phased following excitation and then re-phased at a chosen time known as the echo time (TE). Echoes may be formed through the application of additional RF pulses after excitation (spin echoes) or through manipulation of the linear gradient fields (gradient echoes). Spin echoes are usually acquired for clinical imaging because the radio-frequency refocusing pulses eliminate the signal loss due to local field inhomogeneities ($\Delta B$). The signal in the resulting images depends on $T_2$. In contrast, gradient echoes do not eliminate signal decay owing to $\Delta B$; therefore the signal in gradient echo images depends on the shorter time constant $T_2^*$. However, gradient echoes can be created much more quickly than spin echoes and generally offer higher contrast in functional MRI images. The signal generated by a gradient echo imaging sequence is given by

$$S_{\mathrm{GE}} = M_0 \cdot \sin\,\theta \cdot \frac{1 - \mathrm{e}^{\frac{-TR}{T_1}}}{1 - \cos\,\theta \cdot \mathrm{e}^{\frac{-TR}{T_1}}} \cdot \mathrm{e}^{\frac{-TE}{T_2^*}}, \tag{11.5}$$

where $M_0$ is the initial magnetization, $\theta$ is the flip angle, and TR is the repetition time, a parameter which measures the time between excitations in MR imaging sequences. Flip angle, TR, and TE may be specified by the individual conducting the experiment before scanning.

There exist many imaging sequences in MRI, each designed for a different purpose. For functional brain imaging, we aim to detect small activation-related signal changes very quickly and often use a sequence known as Echo Planar Imaging (EPI). EPI sequences acquire an entire image following a single excitation pulse. Within an excited slice, the signal from all of the spins is encoded with a train of gradient echoes generated by rapidly oscillating frequency-encoding gradients and "blipped" phase-encoding gradients.

The high sampling rate in EPI effectively freezes motion during the scan and allows imaging of dynamic processes in the body with a time series of images. EPI also maximizes the fraction of imaging time devoted to data acquisition and generally provides high signal-to-noise per unit time. On the other hand, the quality of individual EPI images may be rather poor. Because the entire train of gradient echoes is collected within one $T_2^*$ decay envelope, EPI is sensitive to bulk magnetic field inhomogeneities which lead to shifting, geometric distortion, blurring, and signal loss in EPI images [1]. There may also be inconsistencies between gradient echoes obtained with positive vs. negative frequency-encoding gradients; this leads to the so-called Nyquist ghost artifact, in which copies of the true image are shifted and layered on top of it. Together these complications may cause serious artifacts in EPI images or may decrease the stability of a time series of EPI images. However, many of these issues can be addressed with careful sequence optimization or through post-processing. In general the benefits of using EPI sequences for imaging brain function outweigh the drawbacks, and EPI is currently the most widely used sequence for functional brain imaging.

## 2 Principles of Functional MRI

About two decades ago, it was demonstrated that magnetic resonance imaging could be used to noninvasively map changes in neural activity in the brain. In 1990, Ogawa et al. showed that blood with varying levels of oxygen content modulated contrast in a time series of MR images of the rat brain. This blood oxygen level dependent (BOLD) effect was replicated in humans [2–4], and BOLD-based functional magnetic resonance imaging (fMRI) rapidly became a primary research tool for the study of human brain function. In the last twenty years, fMRI has been used to investigate everything from activity in the primary sensory and motor cortices to cognitive functions including attention, language, learning, and memory, to brain disorders ranging from Alzheimer's to autism, and to more (e.g., [5]). Recently it has become clear that fMRI scans of persons at rest can provide insights into how brain regions are networked and how changes in those networks are reflected in behavior and cognition [6–8]. This section describes the principles and methods that make it possible to measure brain function with MRI.

Before going into more detail, it is important to note that BOLD fMRI experiments do not measure neural activity directly, but instead measure differences in the NMR signal related to changes in blood oxygenation near the sites of increased

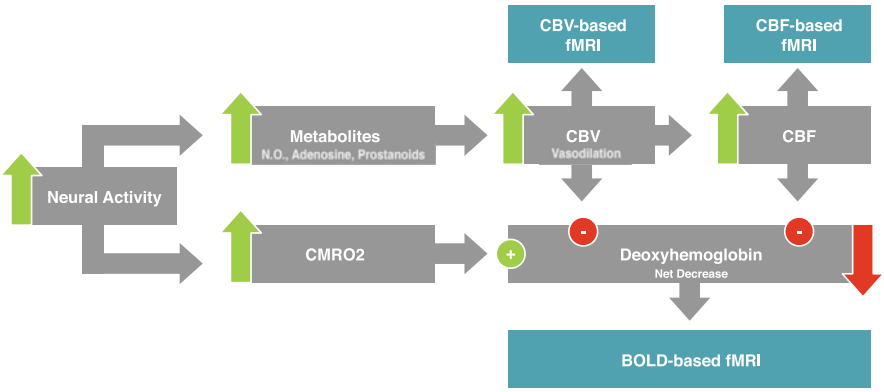


**Fig. 11.4** Schematic representation of the mechanisms behind the various types of functional MRI (CBV, CBF, and BOLD). The source of the BOLD signal is a net decrease in deoxyhemoglobin in blood vessels near the site of neural activity. Even though the slight increase in $CMR_{O2}$ may increase the local deoxyhemoglobin concentration, the more dramatic effects of increased CBV and CBF far outweigh this effect and net dHb is decreased. Other fMRI methods seek to measure changes in CBV and CBF directly

neural activity. A comprehensive description of BOLD-related signal changes depends on complex interactions between several physiological factors including cerebral blood flow (CBF), cerebral blood volume (CBV), and cerebral metabolic rate of oxygen ($CMR_{O2}$). Fig. 11.4 illustrates these relationships schematically.

The mechanisms underlying most BOLD fMRI experiments can be summarized as follows: First, the metabolic process associated with neuronal activity transforms diamagnetic oxyhemoglobin (Hb), which has magnetic properties similar to those of tissue, into paramagnetic deoxyhemoglobin (dHb), which has magnetic properties different from those of tissue. The differences in magnetic susceptibility $(\Delta\chi)$ between compartments which contain dHb (red blood cells within blood vessels) and those which contain only oxygenated Hb (the surrounding area) create small magnetic field gradients which cause local spins to become out of phase and shorten $T_2^*$ near the site of activation. Second, an increase in neural activity induces a significant increase in regional cerebral blood flow (CBF) and cerebral blood volume (CBV) without a commensurate increase in the regional oxygen consumption rate ($CMR_{O2}$) [9, 10]. When the fresh, oxygenated blood arrives at the site of increased activity, the already metabolized paramagnetic dHb is washed away and the local concentration of diamagnetic Hb in veins and capillaries increases significantly. This in turn leads to a significant increase in the local $T_2^*$, which lasts for several seconds and is reflected in increased intensity in images sensitive to $T_2^*$ (or $T_2$).

If a series of $T_2^*$-weighted images is collected while a subject alternates between rest and task conditions, image intensity during task vs. rest can be statistically compared to draw inferences about which brain regions are engaged by the task. Material specific to the design and analysis of fMRI experiments will be covered later in this chapter.

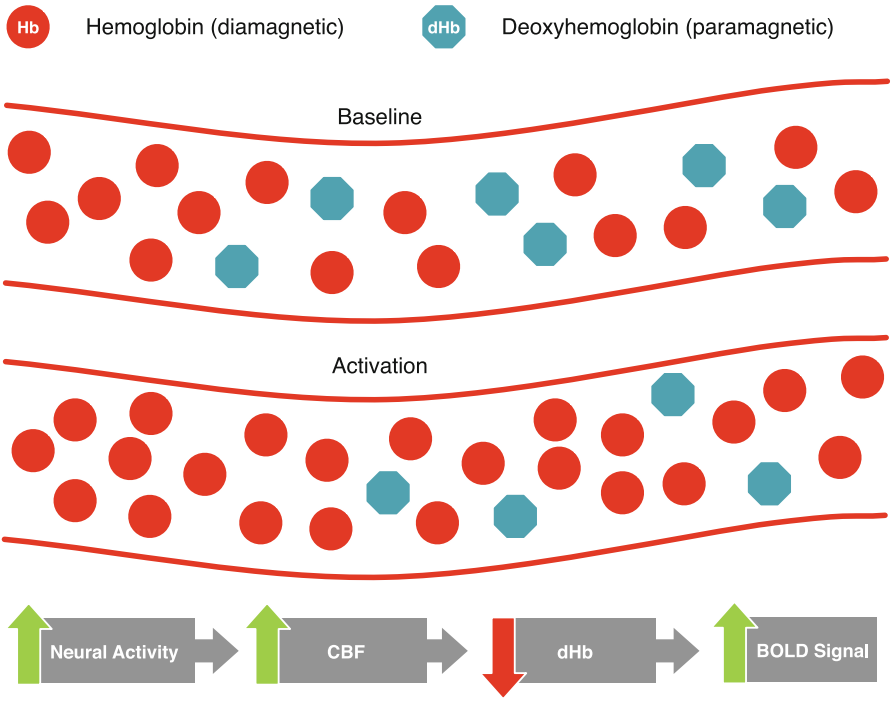


**Fig. 11.5** Illustration of differences between baseline and active states inside blood vessels near the site of neural activity (*top*), together with a simplified schematic of the source of the bold signal from Fig. 11.4 (*bottom*)

Figure 11.4 suggests that CBF and CBV can be used as surrogate measures of brain activity. The measurement of CBF is based on the radio-frequency labeling of water protons in the arterial blood and is often termed arterial spin labeling (ASL). Specifically, ASL uses magnetically labeled arterial blood water as an endogenous tracer for measuring CBF [11]. In this method, arterial blood flowing toward the region of interest (ROI) is labeled by magnetic inversion. After a delay to allow for labeled blood to flow into the ROI, an image is acquired which depends on both the static tissue and the amount of tagged blood that has entered the slice. A control image in which the inflowing blood is not inverted is also acquired. The difference of the labeled image and the control image depends only on blood flow and thus serves as a CBF-weighted image that can be used to calculate absolute CBF.

It is also possible to acquire CBV-weighted images, with or without the use of a contrast agent. The approach without contrast agent detects changes in vascular space occupancy (VASO) by acquiring images when the blood signal is selectively nulled [12]. It provides a means for measuring relative changes in CBV due to brain activation.

Functional activation maps generated with BOLD, CBF, and CBV are mostly similar. However, because BOLD, CBF, and CBV contrasts probe different points

**Table 11.1** Approaches to imaging brain function with MRI

| | BOLD | CBF | CBV |
|---|---|---|---|
| Definition | Mix of CBF, CBV, $CMR_{O2}$ | Blood passing capillary bed in tissue per unit time | Volume of blood in given quantity of tissue |
| MRI approach | T2*-weighting | Arterial spin labeling (ASL) | Contrast agent or vascular space occupancy (VASO) |
| Specificity | Venous bias, susceptibility in surrounding regions | Arterioles/capillaries | Mixed |
| Advantages | Robust | Spatial specificity, reproducibility, quantifiable | Spatial specificity, reproducibility, quantifiable |
| Disadvantages | Poor reproducibility | Low SNR, low sensitivity | Low SNR, low sensitivity |

(and spatial characteristics) in the hemodynamic response process, and because imaging brain function with each of these methods requires a specialized imaging sequence, there are important differences in their properties. In general, BOLD methods have the highest sensitivity and are therefore the most widely used approach for functional brain imaging. However, there are advantages of CBV and CBF approaches, most notably high spatial specificity, reproducibility, and longitudinal consistency [13, 14]. See Table 11.1 for a more detailed comparison of BOLD, CBF, and CBV-based fMRI methods.

## 3 fMRI Experiment Design

Since the BOLD fMRI signal is derived from the hemodynamic response, the design of fMRI studies must take the slow temporal characteristics of this response into account. In light of this, two major types of fMRI study designs have emerged: "block" and "event-related" design (illustrated in Fig. 11.6).

Block design is analogous to the method used in older PET studies, where sustained cognitive or perceptual engagement is required and brain activation is defined by the difference in response between the task and rest/control blocks. In typical block design fMRI, stimulus is presented continuously during the "task" blocks. This is advantageous in that the activity-related signal change observed in block design fMRI is generally quite high. However, several drawbacks relate to the requirement of a sustained stimulus during the "task" blocks. For example, block design precludes the use of many classic psychological paradigms (e.g., the "odd-ball" scheme), may introduce confounding factors such as habituation or expectation, and discards temporal information about individual hemodynamic response functions to specific stimuli. Block design experiments are commonly found in early fMRI studies of visual processing; in one example, O'Craven et al. asked

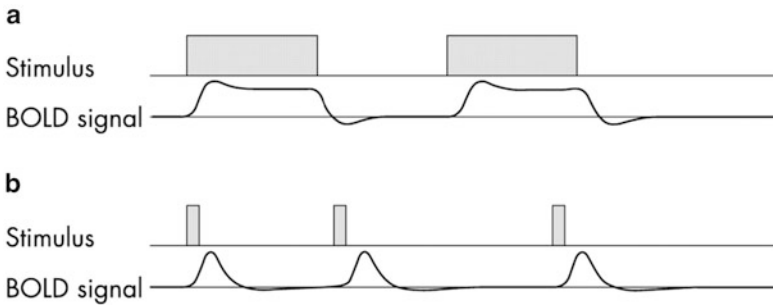


**Fig. 11.6** Schematic diagram of block (**a**) and event-related (**b**) fMRI experiment design (adapted from with permission). In the block design, stimuli or trials are continuously presented in task blocks, yielding cumulated "steady state" BOLD signal during the blocks. In the event-related design, stimuli or trials are presented individually yielding distinguishable hemodynamic responses

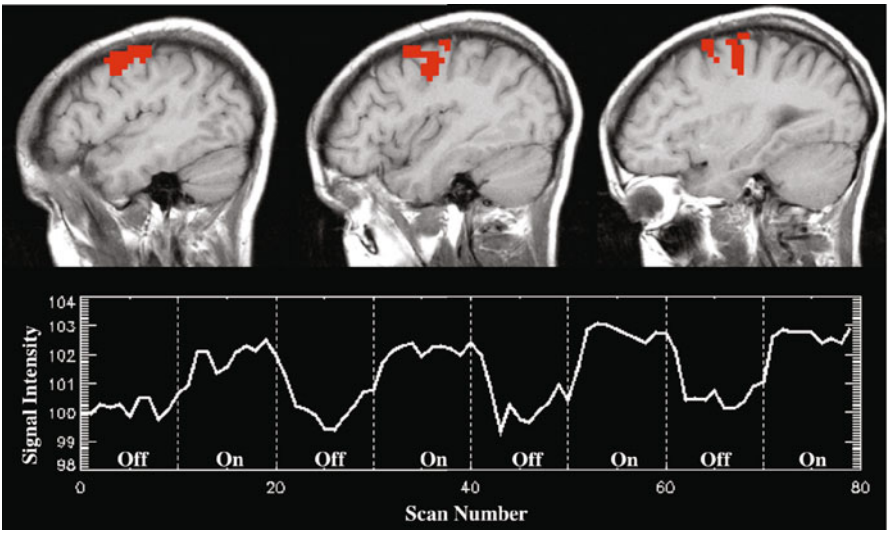


**Fig. 11.7** Activation map (*top*) and signal time course (*bottom*) for a finger-tapping task [courtesy of Yihong Yang, National Institute on Drug Abuse (NIDA)]

subjects to pay attention to static or moving dots in different task blocks and observed attentional modulation of neural activity in the MT region [15]. As another example, Fig. 11.7 shows activation maps and the corresponding block design paradigm for a simple finger-tapping task.

Event-related design is used in situations where the brain responses to single trial/stimulus or the temporal details of the brain responses are of interest. In event-related designs, stimuli are presented individually and the corresponding hemodynamic responses are measured separately (Fig. 11.6). The time between stimuli (known as

the inter-stimulus-interval (ISI) or inter-trial-interval (ITI)) can be used to further categorize event-related designs into "spaced" and "rapid" single trial approaches. The "spaced" design usually uses a long ISI/ITI (typically more than 10 s) to allow full hemodynamic response recovery so that signals of successive stimulus/trial are fully separated, while the "rapid" design uses short ISI/ITI (typically 2–5 s) to improve experiment efficiency. In rapid design, the responses of successive stimulus/trial are overlapped; this requires a linear deconvolution post-processing step to separate the BOLD responses [16]. Examples of event-related fMRI are easily found in studies of error monitoring (e.g., [17]). Errors occur unpredictably by nature and therefore must be examined in the context of an event-related design. More details regarding fMRI experiment design can be found in Amaro and Barker [18].

## 4 fMRI Data Analysis

The power of fMRI lies in our ability to form an association between BOLD signal variation, external sensory input, and brain function. This can be achieved by analyzing the fMRI signal with statistical and mathematical techniques. However, many artifacts and noise sources may compromise the integrity of fMRI data; we must therefore remove such artifacts before we can conduct meaningful analysis on it. The steps between image reconstruction and data analysis are collectively known as preprocessing.

### *4.1 Preprocessing*

The goal of preprocessing procedures is to reduce unwanted variability in the experimental data and to improve the validity of statistical analyses. Some common fMRI data processing steps include: motion correction to ensure registration throughout a time series of images which may have been collected over several minutes [19]; "slice timing" correction of phase differences between slices acquired at significantly different times in multi-slice acquisitions like EPI [20, 21]; distortion correction to ensure adequate registration of functional activity to associated anatomical images [22, 23] and spatial smoothing to increase image SNR and improve signal detection capabilities at the cost of subject-specific activation information. Figure 11.8 (adapted from [24]) shows the basic framework for preprocessing of fMRI data, where most steps outlined are introduced in this section.

Many common artifacts can be detected by directly examining raw functional images. One effective way of viewing raw data is to display slices in a rapid sequence and using the human eye's sensitivity to dynamic change to detect artifacts. Statistical tests such as measurements of mean image intensity, principal component analysis (PCA), and independent component analysis (ICA) may also be used to evaluate the quality of collected fMRI data.

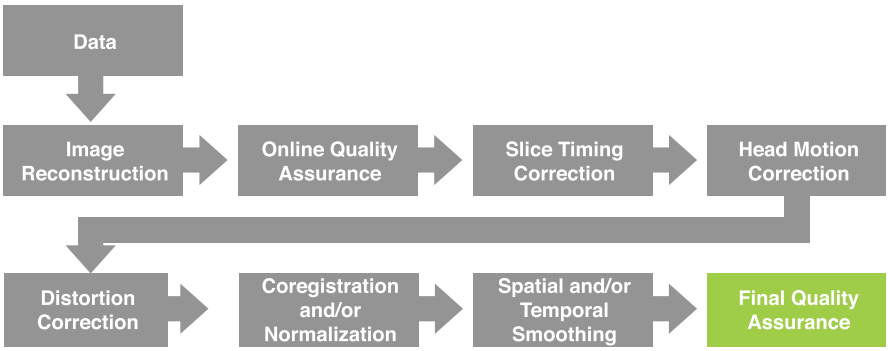


**Fig. 11.8** Schematic framework for preprocessing of fMRI data with an interleaved slice acquisition scheme. In a sequential slice acquisition scheme, Head Motion Correction and Slice Timing Correction are reversed

### 4.1.1 Motion Correction

Motion correction aims to ensure that each voxel stays in the same spatial location throughout the duration of data acquisition. Because the brain does not change size and shape (it merely shifts and rotates as the head moves), rigid body transformation methods are often used for retrospective correction of head motion in fMRI. Successive image volumes in the time series are co-registered to a single reference volume by first determining the six variables of rigid body transformation (three rotations and three translations) and then performing interpolation according to these six parameters. Each of the main fMRI data analysis packages (SPM [24], FSL [25], AFNI [26], and Brain Voyager [27]) has implemented their own approach to motion correction. In cases of excessive motion (shifts on the order of several voxels), the data may not be usable for further analysis. It is therefore common practice to limit physical head motion during data acquisition with head-immobilization techniques such as a strap restraint, bite bar, or foam padding.

### 4.1.2 Slice Timing Correction

In a given MR data volume acquisition time (typically 1–3 s), the slices within a volume are collected either sequentially or in an interleaved manner (e.g., odd slices followed by even slices). If the relative acquisition time of each slice is not taken into account, the time courses for each slice would appear to vary dramatically even if the underlying activity is identical. To address this issue, temporal interpolation algorithms (mostly sinc interpolation) are often employed. These algorithms use information about nearby slices to estimate the signal that would have been obtained at the same time as the reference slice. The interpolated time point is typically chosen as TR/2 to minimize relative errors across each TR.

### 4.1.3 Functional–Structural Co-registration

Functional co-registration aims to align an fMRI time series with a high-resolution structural MR image. Because the size, shape, and sulcus patterns of the brain are much more distinct on structural images, it is beneficial to use information from these images to locate subject's task activation area and guide normalization of functional images. After motion correction, a mean fMRI scan is calculated and used in the functional–structural co-registration. An affine (twelve parameters) functional MRI–structural MRI transformation can allow for scaling between the two image types. Cost functions based on mutual information are considered optimal for fMRI–MRI registration [28].

### 4.1.4 Normalization

Human brains differ in size, shape, and organization of cortical structures. To compare the areas of activation across different subjects, we must be able to study such activation in a common spatial coordinate system. This process, known as normalization, is a form of co-registration which uses mathematical stretching, squeezing, and warping to bring brains into common frame of reference. Currently, the most widely used template is the Talairach system which is based on a single brain [29]. Recently a more sophisticated template, derived from the anatomies of over a hundred subjects, has become available. This template is developed by the researchers at the Montreal Neurological Institute (MNI) and is called the MNI space [30]. Within MNI space, the most common normalization algorithms are cost functions using surface-based landmarks or voxel-based intensities; of these, the latter is most widely used.

### 4.1.5 Temporal Filtering

In fMRI data analysis, we are generally interested in signal changes related to a specific task. Therefore we need to minimize or filter out the influence of undesired noise. Depending on what sort of variability should be eliminated, different kinds of temporal filters (low-pass, band-pass, etc.) can be selected. For example, the human heart rate generally varies between 1.0 and 1.5 Hz. For a block design experiment with two alternating blocks of 20-s length, the task rate is 0.05 Hz. In this situation, a low-pass filter with cutoff frequency less than 1.0 Hz would remove the physiological oscillations without significantly reducing the ability to detect the task effect of interest.

Generally, temporal filtering is used for physiological noise correction, removing thermal noise, and estimation of temporal autocorrelations. The use of temporal filters can substantially improve the quality of fMRI data by improving functional signal-to-noise ratio (SNR).

### 4.1.6 Spatial Filtering

The blurring of fMRI data across adjacent voxels to improve the validity of statistical testing and maximizing functional SNR is called spatial smoothing or spatial filtering. A Gaussian smoothing kernel of 1–2 voxels full width half maximum is usually used. While spatial smoothing can increase the SNR and provide cleaner activation maps, it does so at the price of spatial resolution and therefore the ability to associate a given area of activity with a specific anatomical feature. The extent of spatial smoothing is largely depends on the desired application. If precise spatial discrimination of adjacent activation sites is required, one should be conservative with spatial smoothing; on the other hand, if coarse but clean activation maps are desired and/or the SNR is very low due to a subtle cognitive effect, more spatial smoothing may be appropriate [31–33].

## *4.2 Statistical Tests*

A fundamental assumption of fMRI is that regions in the brain which activate in response to a given stimuli must show signal variation that is similar in some way to the external input. The extent to which the fMRI signal at various locations and external stimulus are similar (or dissimilar) can be judged by statistical analysis of the fMRI time series data. Types of statistical analysis commonly applied to fMRI research include t-test, correlation analysis, and regression analysis.

### 4.2.1 t-Test

A t-test is generally used to test the hypothesis that the mean of a sample is different from a specific value or that the means of two different samples are different from one another. Suppose there is a blocked design with two conditions: task and rest. To conduct a t-test in this design, the means of the data from these two conditions are subtracted and then divided by the shared standard deviation:

$$t = \frac{\bar{x} - \bar{y}}{\sigma_{xy}} = \frac{\bar{x} - \bar{y}}{\sqrt{\sigma_x^2 + \sigma_y^2}}, \tag{11.6}$$

where $x$ represents the data of a given voxel acquired during the task condition, and $y$ represents data of that voxel acquired during rest. The standard deviations of the time courses $x$ and $y$ are given by $\sigma_x$ and $\sigma_y$, respectively.

The calculated t-value can be converted to a probability value by dividing it by the number of degrees of freedom. By comparing the calculated probability value

with the set alpha value, we can then decide whether or not to reject the null hypothesis. For example, suppose the calculated probability value is 0.001; this means there is a 0.001 chance that the data in these conditions were drawn from the same distribution. If the alpha value is set to be 0.01, the probability value is lower than the threshold alpha value, and thus the null hypothesis can be rejected.

### 4.2.2 Correlation Analysis

One way of ascertaining the similarity of the external stimulus (and hence the predicted hemodynamic response) and the measured fMRI signal from a voxel is by employing the correlation coefficient. If the experimental data are represented by $x$, and the predicted response is represented by $y$, then the correlation coefficient between the measured and predicted response is given by

$$r = \frac{1}{n-1} \cdot \frac{\Sigma(x-\bar{x})(y-\bar{y})}{\sigma_x \cdot \sigma_y}, \tag{11.7}$$

where the numerator is the covariance of the two data sets and $\sigma_x$ and $\sigma_y$ are the standard deviations. The correlation value ($r$) can be converted to a probability value in the same way as with a t-test, and the probability value may then be compared with an alpha value. This correlation analysis is repeated for each voxel in the brain to obtain a map of significant task-related signal changes. The t-test and correlation analysis have complementary strengths. The former allows us to evaluate contrasts between experimental conditions, whereas the latter allows us to create models for expected fMRI activation.

### 4.2.3 Regression Analysis: The General Linear Model

The t-test and correlation analyses are suitable for comparing a limited number of conditions. If the comparison is between multiple conditions resulting in many contrasts, regression analysis is more suitable. With regression analysis, it is also possible to model nuisance variables and hence increase the power to detect activation.

In regression analysis, the observed data are treated as a linear combination of several regressors plus the residual noise (error) in the measurement. For each regressor, there is a weighting coefficient which determines the relative influence of that regressor on the data model. One of the most popular types of regression analysis used in fMRI experiments is the General Linear Model (GLM). The general linear model assumes a linear relationship between the measured data and the task-induced changes, such that

$$y(t) = \beta_i \cdot x_i(t) + c + e(t), \tag{11.8}$$

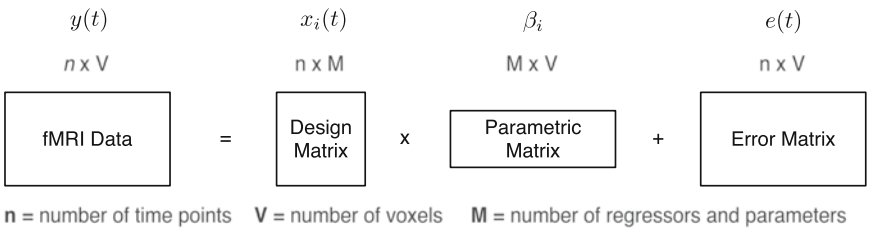


**Fig. 11.9** Schematic of the general linear model as applied in fMRI

in which the subscript $i$ counts the number of regressors in the model, and where $y(t)$ is the time series of a given voxel, $x(t)$ is a regressor of interest (i.e., a task), $c$ is a constant, and $e(t)$ is the residual error of the model which accounts for variance in $y(t)$ which cannot be explained by the linear model [34, 35]. Beta weights $\beta$ are commonly estimated through an ordinary least squares fit to the GLM and are used to determine the significance of activation (commonly measured as T- or F-statistics).

Figure 11.9 shows an illustration of the general linear model. In GLM analysis for fMRI, the acquired data become a two-dimensional matrix $Y$, with $V$ columns representing the tested voxels, and $n$ rows representing the time points per voxel. The data matrix is known since it is obtained experimentally. The design matrix is composed of the regressors, and is an $n$-by-$M$ matrix where each column represents a regressor, and each row represents the time course of that regressor. The design matrix is constructed based on knowledge of the stimuli and the predicted responses of the experiment. The parametric matrix is an $M$-by-$V$ matrix in which each volume of beta represents certain weighted coefficients of all the regressors for a corresponding voxel. Finally, the error matrix is an $n$-by-i matrix which captures the variance in the data which cannot be explained by the design and parametric matrices. The primary task of GLM analysis is to calculate the optimal parameter matrix so that some cost function of the error matrix is minimized.

Note that in both GLM and correlation analysis, we calculate activation significance based on how well the experimental data fit a prediction. If the general linear model only contains one regressor which is calculated by the convolution of events with a standard hemodynamic response, then this GLM model resembles the correlation analysis. The $t$-test can be incorporated into the general linear model by using only one regressor with two discrete levels: one for the task condition and the other for the rest condition in an alternating blocked design.

## 5 Biophysical Modeling of the fMRI Signal

As mentioned above, BOLD-based fMRI depends on changes in the concentration of oxygenated and deoxygenated hemoglobin. In the brain, hemoglobin stays within blood vessels and its effects must be considered in that context.

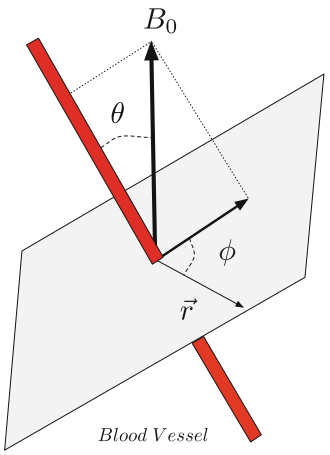


**Fig. 11.10** A blood vessel in a static magnetic field. The labeled parameters determine the susceptibility effect induced by deoxyhemoglobin in red blood cells at a distance $r$ from the center of the vessel. The vessel with radius $a$ is oriented at angle $\theta$ from the main magnetic field $B_0$, and $\phi$ is the angle between $r$ and a plane defined by $B_0$ and the vessel axis

If one considers an infinite cylinder as an approximation for a blood vessel with a magnetic susceptibility difference $\Delta\chi$ compared to the surrounding tissue, then the magnetic field surrounding that cylinder (expressed in resonance frequency) will be perturbed from the applied magnetic field $\omega_0$ in proportion to the local magnetic susceptibility gradients. Inside the vessel, intravascular (IV) perturbation is given by

$$\Delta\omega_B^{\text{in}} = 2\pi\Delta\chi_0(1-Y)\,\omega_0\left(\cos^2\theta - \frac{1}{3}\right), \tag{11.9}$$

while at any point outside the cylinder the magnetic field will vary depending on the distance and orientation relative to the blood vessel and the external magnetic field direction. This field extravascular (EV) perturbation is given by

$$\Delta\omega_B^{\text{out}} = 2\pi\Delta\chi_0(1-Y)\;\;\omega_0\left(\frac{r_b}{r}\right)^2\sin^2(\theta)\cos(2\phi), \tag{11.10}$$

where $\Delta\chi_0$ is the maximum susceptibility difference expected in the presence of fully deoxygenated blood, $Y$ is the fraction of oxygenated blood present, $r_b$ represents the cylinder radius, and $r$ is the distance from the point of interest to the center of the cylinder in the plane normal to the cylinder. These relationships are illustrated in Fig. 11.10.

The dephasing effect is dependent on the orientation of the vessel. Vessels running parallel to the magnetic field do not have the EV effect, while those orthogonal to $B_0$ will have maximal effect. Outside the blood vessel, the magnetic field changes rapidly; at a distance equal to the diameter of the cylinder from the cylinder center, $\omega_B^{\text{out}}$ is already down to 25% of its value at the cylinder boundary.

$T_2^*$-based BOLD signal changes can arise both from intravascular and extravascular effects originating from both large and small blood vessels. The relative contributions of these effects will depend on the magnetic field strength [36].

BOLD contrast relies on monitoring oxygen concentration in the blood (particularly venous blood). It is therefore intimately related to CBF, cerebral metabolic rate of oxygen ($CMR_{O2}$), and cerebral blood volume (CBV) as shown in Fig. 11.6. The interplay between these three physiological parameters determines the BOLD response and can be described in a phenomenological manner as follows:

$$\Delta R_2^* = -\frac{\Delta \mathrm{BOLD}}{\mathrm{BOLD}} \cdot \frac{1}{TE} = -\alpha^* \left\{ \frac{\Delta Y}{1-Y} - \beta^* \frac{\Delta \mathrm{CBV}}{\mathrm{CBV}} \right\}, \tag{11.11}$$

where $\alpha^*$ and $\beta^*$ are constants ($\alpha$ is typically assumed to be 0.38), and $Y$ is the oxygenation content of the blood [37]. The change in the oxygenation level $\Delta Y$ is related to the changes of $CMR_{O2}$ and CBF as follows:

$$\frac{\Delta Y}{1-Y} = 1 - \frac{1 + \frac{\Delta \mathrm{CMR_{O2}}}{\mathrm{CMR_{O2}}}}{1 + \frac{\Delta \mathrm{CBF}}{\mathrm{CBF}}}. \tag{11.12}$$

With measurements of $\Delta R^*$ and $\Delta$ CBF, the above equations can be used along with the Grubb's relationship [38], which quantifies the effects of changes in arterial carbon dioxide tension on CBV, CBF, and vascular mean transit time, to estimate $\Delta \mathrm{CMR_{O2}}$.

Various models have been proposed to estimate $\Delta \mathrm{CMR_{O2}}$ from fMRI measurements. For instance, the balloon model [39] assumes that CBV changes occur predominantly in the venous compartment and that the CBF increase induced by neuronal activity is accompanied by an increase in $\Delta \mathrm{CMR_{O2}}$ which causes an increase followed by a subsequent decrease in CBV.

Similarly, the deoxyhemoglobin dilution model [11, 40] replaces the assumption of numerous parameters with a single parameter (M) that can be measured experimentally using the following:

$$\frac{\Delta \mathrm{BOLD}}{\mathrm{BOLD}} = M \cdot \left( 1 - \left( \frac{\mathrm{CMR_{O2}}}{(\mathrm{CMR_{O2}})_0} \right)^{\beta} \cdot \left( \frac{\mathrm{CBF}}{\mathrm{CBF_0}} \right)^{\alpha - \beta} \right), \tag{11.13}$$

where $\beta$ is a constant reflecting the influence of deoxyhemoglobin concentration. For this approach, BOLD and CBF are measured at various levels of deoxyhemoglobin concentration and hypercapnia ($\alpha$, inhaled $CO_2$ concentrations typically ranging from 1 to 5%) and the data are fit to yield a value of the calibration parameter M that is specific to a given subject, day, brain region, and so on. More sophisticated models with similar assumptions have recently been presented [41–43], as well as approaches for estimating CBV directly from MR measurements instead of assuming Grubb's relationship [37].

Another model assumes multiple compartments, separating the BOLD signal into intravascular (30% arteriole, 70% venule) and extravascular components. Instead of relying on calibration, this approach utilizes task-related BOLD and

CBV changes to calculate oxygen extraction fraction (OEF) as a means to estimate $CMR_{O2}$ [44]:

$$\left(1+\frac{\Delta \mathrm{OEF}}{\mathrm{OEF}}\right)\cdot\left(1+\frac{\Delta \mathrm{CBF}}{\mathrm{CBF}}\right)=\left(1+\frac{\Delta CMR_{O2}}{\mathrm{CMR_{O2}}}\right). \tag{11.14}$$

However, non-contrast studies typically require the assumption of resting CBV levels as well as the measurement of VASO signal changes during activation. Ultimately, further studies will evaluate the extent to which each of these methods are accurate and have acceptable assumptions.

## 6 Spatial and Temporal Resolutions

Depending on the application, low-resolution coverage of the entire brain or high-resolution coverage of certain brain areas may be desirable. Most fMRI experiments at 3 T employ single-shot EPI with about 30 slices of matrix size 64 × 64 or 80 × 80 with 3 mm × 3 mm × 3 mm voxels in about 2.5 s [5]. However, with the advent of high field human scanners operating at 7 T and above, imaging at much higher spatial resolutions has become possible. Higher magnetic field strengths increase the baseline signal which in turn allows higher spatial resolutions (and therefore more precise illustrations of the organization and topography in the human brain) to be achieved with reasonable SNR. Figure 11.11 shows maps of the primary visual cortex (V1) acquired at resolutions of 1.67 mm × 1.67 mm × 1.67 mm and 1.12 mm × 1.12 mm × 1.12 mm at 7 Tesla.

Two major physiological factors contribute to the achievable spatial resolution of fMRI studies. One is the sensitivity of the chosen imaging sequence to blood vessels of different sizes, and the second is the actual spatial specificity of the BOLD-related events that ultimately yield the functional images.

Beyond the nominal voxel size, the achievable spatial resolution of fMRI is dependent on intrinsic hemodynamic response as well as SNR. Both factors will determine the accuracy of the functional map.

Since the BOLD signal is related to changes in blood flow, the inherent temporal resolution of fMRI is tied to the timescale of this hemodynamic response (on the order of seconds) and not changes in neural activity (which occur on a scale of milliseconds) [45]. Therefore it can be difficult to obtain high temporal resolution information about brain function from BOLD data even when the MR images themselves are obtained rapidly.

Typically, hemodynamic signal changes are observed at 1–2 seconds after the onset of neuronal stimulation and reach a maximum after 4–8 seconds. The precise timing of neural activity relative to the hemodynamic responses cannot be easily obtained because the hemodynamic response varies depending on local vascular structures. If the hemodynamic response times in all regions in all subjects were the same, neuronal activities could be directly inferred from fMRI time courses. However, this may not be

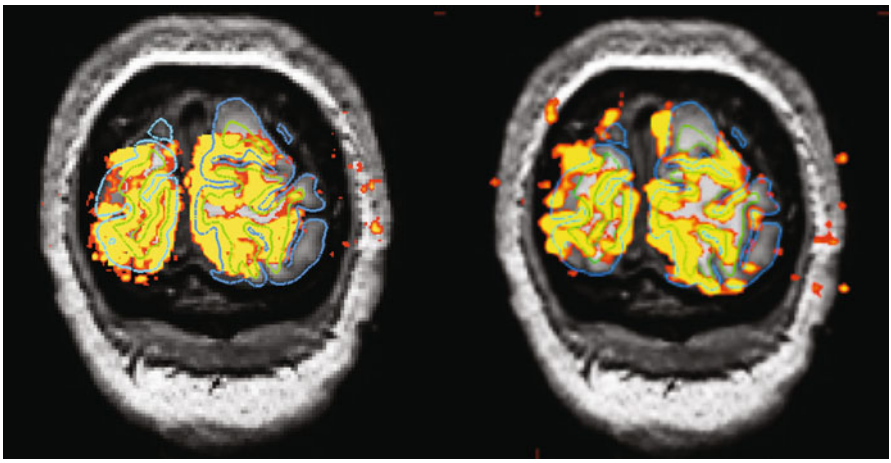

**Fig. 11.11** Activation maps of the primary visual cortex (V1) acquired with EPI at 1.12 × 1.12 × 1.12 $mm^3$ (*left*) and 1.67 × 1.67 × 1.67 $mm^3$ (*right*) on a 7 T scanner. *Blue lines* represent the edges of the cortical surface, while *green lines* represent the *gray*/*white* matter boundary. Notice that some activation appears distorted off of the cortical surface; this is an example of a magnetic susceptibility effect as described previously (images courtesy Jascha Swisher, Vanderbilt University Institute of Imaging Science)

true in all regions and in all subjects, and thus apparent differences in fMRI time courses may simply be related to differences in intrinsic hemodynamic response time rather than the timing of neuronal activity. This is critically important when attempting to determine, for example, the sequence of neural events when one area in a network of brain regions may be driving activity in other regions [46].

## 7 Signal and Noise Considerations

In a functional MRI experiment, images must be acquired quickly to adequately sample the hemodynamic response to brain activity. The fast speed at which these images must be acquired also means the SNR of individual images in an fMRI time series tends to be low. To make up for this, many images are generally obtained in both "task" and "rest" conditions. Differences in signal between the two are then compared to a measure of temporal signal variance and significant differences between "task" and "rest" are then determined by statistical tests. Because the signal changes associated with BOLD fMRI are so small, high temporal signal stability is critical to BOLD fMRI experiments. The temporal signal-to-noise ratio (TSNR) is defined as the mean value of a signal within a single voxel compared to the standard deviation of the signal in that voxel over time in a series of images:

$$TSNR = \frac{\bar{S}}{\sigma}. \tag{11.15}$$

Several noise components contribute to the total signal variation in a time series of images. These include time-varying thermal noise ($\sigma_T$), noise caused by system instability ($\sigma_S$) and, in living subjects, physiological noise from metabolic, cardiac, or respiratory activity and related motion ($\sigma_P$). When these are independent the total noise may be written as follows:

$$\sigma = \sqrt{\sigma_T^2 + \sigma_S^2 + \sigma_P^2}. \tag{11.16}$$

First identified by Weisskoff et al. in 1993, physiological noise ($\sigma_P$) is now known to be a dominant source of temporal signal variation in fMRI time series data. Physiological noise depends on the NMR signal and therefore increases with magnetic field strength and voxel volume [47, 48]. Numerous techniques for physiological noise removal have been suggested, including navigator echoes, retrospective gating, digital filtering, k-space and image-space based estimation, pulse sequence gating, and more [49–54].

## 8 Combining fMRI and EEG for Human Brain Mapping

Localizing neural activities in the brain, both in time and in space, is a central challenge to understanding functional brain mechanisms. However, even with a variety of modern neuroimaging modalities available (electroencephalography (EEG), magnetoencephalography (MEG), positron emission tomography (PET), single photon emission computed tomography (SPECT), and fMRI), no single approach can claim the highest resolution in both space and time for all experimental or clinical conditions. BOLD fMRI can map brain activity with a spatial resolution on the order of millimeter, but since BOLD fMRI relies on the hemodynamic response this technique can only provide slow, temporally blurred information about the underlying neuronal activity. In contrast, EEG (or MEG) can directly capture electrical or magnetic signals associated with active neurons in real time, but because those signals are measured through the scalp, the recorded signal is a spatially blurred mixture of underlying neural "sources" and thus has limited spatial resolution.

Given the complementary strengths and weaknesses of fMRI and EEG, many researchers are working to bring these two modalities together to achieve high-resolution data in both space and time simultaneously. Early attempts at such temporal–spatial data integration can be found in studies of cognitive attention; for example, Heinze and colleagues explored the cortical anatomy and time course of attentional selection [55]. In this study, temporal and spatial information was acquired with EEG and PET, respectively, in separate sessions. Multimodal data acquisition is especially desirable in clinical studies of brain diseases such as epilepsy, where researchers commonly use EEG to record epileptic discharges and use fMRI to examine their hemodynamic correlates [56]. As such discharges are usually unpredictable, these EEG and fMRI data must be acquired simultaneously and then

analyzed in the context of an event-related design where events measured on EEG are used as markers in fMRI data analysis.

The fundamental assumption behind any EEG–fMRI integration is that the signals of both modalities are (at least partly) produced by the same neural sources. However, experiments with separate EEG and fMRI recording may violate this assumption as different circumstances regarding stimulation, habituation, or emotion may involve different neural activities. Even with simultaneous recording, differences in the physiological nature of EEG (electrical activity from neurons) and fMRI signal (hemodynamic response) could make one modality blind to signals detected by the other. These different signals may also arise from physically separate locations in the brain [57]. Other confounds include the possibility that nonelectrical, energy-consuming physiological processes (e.g., neurotransmitter synthesis) may produce BOLD signal changes invisible to EEG [58], or that transient electrical activity may produce EEG signals invisible to fMRI [59]. These and other issues surrounding the integration of fMRI and EEG data are explored in detail Chapter 12.

## 9 Summary

Functional magnetic resonance imaging is widely used for noninvasively mapping brain activity. The methods and applications of fMRI continue to expand rapidly as new approaches such as measuring functional connectivity in brain networks, tracking information flow in the brain, and integration with EEG and other neuroimaging techniques become widespread. This chapter has introduced the principles of magnetic resonance imaging and functional MRI, examined the biophysical basis of the fMRI signal, and given an overview of fMRI experiment design and data analysis. The interested reader is invited to browse the literature for numerous examples of fMRI applied to fields as diverse as psychology, art, music, economics, medicine, and more.

## References

1. Raj D, Paley DP, Anderson AW, Kennan RP, Gore JC (2000) A model for susceptibility artefacts from respiration in functional echo-planar magnetic resonance imaging. Phys Med Biol 45:3809–3820
2. Bandettini PA, Wong EC, Hinks RS, Tikofsky RS, Hyde JS (1992) Time course EPI of human brain function during task activation. Magn Reson Med 25:390–398
3. Kwong KK, Belliveau JW, Chesler DA, Goldberg IE, Weisskoff RM, Poncelet BP, Kennedy DN, Hoppel BE, Cohen MS, Turner R (1992) Dynamic magnetic resonance imaging of human brain activity during primary sensory stimulation. Proc Natl Acad Sci USA 89:5675–5679
4. Ogawa S, Tank DW, Menon R, Ellermann JM, Kim SG, Merkle H, Ugurbil K (1992) Intrinsic signal chances accompanying sensory stimulation: functional brain mapping with magnetic resonance imaging. Proc Natl Acad Sci USA 89:5951–5955
5. Bandettini PA (2007) Functional MRI today. Int J Physchophys 63(2):138–145

6. Craddock CR, Holtzheumer PE, Hu XP, Maybeg HS (2009) Disease state prediction from resting state functional connectivity. Magn Reson Med 62:1619–1628
7. Friston KJ (1994) Functional and effective connectivity in neuroimaging: a synthesis. Hum Brain Mapp 2:56–78
8. Rubinov M, Sporns O (2010) Complex network measures of brain connectivity: uses and interpretations. Neuroimage 52:1059–1069
9. Fox PT, Raichle ME (1986) Focal physiological uncoupling of cerebral blood flow and oxidative metabolism during somatosensory stimulation in human subjects. Proc Natl Acad Sci USA 83:1140–1144
10. Fox PT, Raichle ME, Mintun MA, Dence C (1988) Nonoxidative glucose consumption during focal physiologic neural activity. Science 241:462–464
11. Hoge RD, Atkinson J, Gill B, Crelier GR, Marrett S, Pike GB (1999) Investigation of BOLD signal dependence on cerebral blood flow and oxygen consumption: the deoxyhemoglobin dilution model. Magn Reson Med 42(5):849–863
12. Lu H, Golay X, Pekar JJ, Van Zijl PC (2003) Functional magnetic resonance imaging based on changes in vascular space occupancy. Magn Reson Med 50(2):263–274
13. Li CW, Wu C-W, Chen D-Y, Chen J-H (2007) Using EPI-based T1 mapping to Compare Activation Localization on Cortical Gray Matter among Three fMRI Techniques: BOLD, FAIR and VASO. Proc IFMBE 14(15):2260–2263
14. Tjandra T, Brooks JC, Figueiredo P, Wise R, Matthews PM, Tracey I (2005) Quantitative assessment of the reproducibility of functional activation measured with BOLD and MR perfusion imaging: implications for clinical trial design. Neuroimage 27(2):393–401
15. O'Craven KM, Rosen BR, Kwong KK, Treisman A, Savoy RL (1997) Voluntary attention modulates fMRI activity in Human MT-MST. Neuron 18:591–598
16. Glover GH (1999) Deconvolution of impulse response in event-related BOLD fMRI. Neuroimage 9:416–429
17. Braver TS, Barch DM, Gray JR, Molfese DL, Snyder A (2001) Anterior cingulate cortex and response conflict: effects of frequency, inhibition and errors. Cereb Cortex 11:825–836
18. Amaro E, Barker GJ (2006) Study design in fMRI: basic principles. Brain Cogn 60:220–232
19. Friston KJ, Williams S, Howard R, Frackowiak RS, Turner R (1996) Movement-related effects in fMRI time-series. Magn Reson Med 35(3):346–55
20. Friston KJ, Josephs O, Rees G, Turner R (1998) Nonlinear event-related responses in fMRI. Magn Reson Med 39(1):41–52
21. Van De Moortele PF, Pfeuffer J, Glover GH, Ugurbil K, Hu X (2002) Respiration-induced B0 fluctuations and their spatial distribution in the human brain at 7 Tesla. Magn Reson Med 47:888–895
22. Jezzard P, Clare S (1999) Sources of distortion in functional MRI data. Hum Brain Mapp 8:80–85
23. Hutton C, Bork A, Josephs O, Deichmann R, Ashburner J, Turner R (2002) Image distortion correction in fMRI: a quantitative evaluation. Neuroimage 16:217–240
24. Huettel SA, Song AW, McCarthy G (2004) Functional Magnetic Resonance Imaging. Sinauer Assoc, Sunderland, Massachusetts
25. Menon RS (2002) Post-acquisition suppression of large-vessel BOLD signals in high-resolution fMRI. Magn Reson Med 47(1):1–9
26. Rowe D (2005) Modeling both the magnitude and phase of complex-valued fMRI data. Neuroimage 25(4):1310–1324
27. Rowe D (2005) Parameter estimation in the magnitude-only and complex-valued fMRI data models. Neuroimage 25(4):1124–1132
28. Freire L, Roche A, Mangin JF (2002) What is the best similarity measure for motion correction in fMRI time series? IEEE Trans Med Imag 21(5):470–484
29. Talairach J, Tournoux P (1988) Co-Planar Stereotaxic Atlas of the Human Brain. Georg Theme Verlag, Stuttgart, Germany

30. Brett M, Johnsrude IS, Owen AM (2002) The problem of functional localization in the human brain. Nat Rev Neurosci 3(3):243–249
31. Friston KJ, Worsley KJ, Frackowiak RSJ, Mazziotta JC, Evans AC (1993) Assessing the significance of focal activations using their spatial extent. Hum Brain Mapp 1(3):210–220
32. Poline JB, Mazoyer BM (1994) Enhanced detection in brain activation maps using a multifiltering approach. J Cereb Blood Flow Metab 14(4):639–642
33. Worsley KJ, Marrett S, Neelin P, Evans AC (1996) Searching scale space for activation in PET images. Hum Brain Mapp 4(1):74–90
34. Friston KJ, Holmes AP, Worsley KJ, Poline JP, Frith CD, Frackowiak RSJ (1994) Statistical parametric maps in functional imaging: a general linear approach. Hum Brain Mapp 2(4):189–210
35. Friston KJ, Holmes AP, Poline JB, Grasby PJ, Williams SC, Frackowiak RS, Turner R (1995) Analysis of fMRI time-series revisited. Neuroimage 2(1):45–53
36. Yacoub E, Van De Moortele PFV, Shmuel A, Ugurbil K (2005) Signal and noise characteristics of Hahn SE and GE BOLD fMRI at 7 T in humans. Neuroimage 24:738–750
37. Lin A-L, Fox PT, Yang Y, Lu H, Tan L-H, Gao J-H (2008) Evaluation of MRI models in the measurement of CMRO2 and its relationship with CBF. Magn Reson Med 60(2):380–389
38. Grubb RL Jr, Raichle ME, Eichling JO, Ter-Pogossian MM (1974) The effects of changes in PaCO2 on cerebral blood volume, blood flow, and vascular mean trainsit time. Stroke 5:630–639
39. Buxton RB, Wong EC, Frank LR (1998) Dynamics of blood flow and oxygenation changes during brain activation: the balloon model. Magn Reson Med 39:855–864
40. Davis TL, Kwong KK, Weisskoff RM, Rosen BR (1998) Calibrated functional MRI: mapping the dynamics of oxidative metabolism. Proc Natl Acad Sci USA 95(4):1834–1839
41. Buxton RB, Uludag K, Dubowitz DJ, Liu TT (2004) Modeling the hemodynamic response to brain activation. Neuroimage 23(Suppl 1):S220–S233
42. Friston KJ, Mechelli A, Turner R, Price CJ (2000) Nonlinear responses in fMRI: the balloon model, Volterra kernels, and other hemodynamics. Neuroimage 12(4):466–477
43. Sotero RC, Trujillo-Barreto NJ, Jimenez JC, Carbonell F, Rodriguez-Rojas R (2009) Identification and comparison of stochastic metabolic/hemodynamic models (sMHM) for the generation of the BOLD signal. J Comput Neurosci 26(2):251–269
44. Lu H, Golay X, Pekar JJ, Van Zijl PC (2004) Sustained post-stimulus elevation in cerebral oxygen utilization after vascular recovery. J Cereb Blood Flow Metab 24(7):764–770
45. Kim SG, Richter W, Ugurbil K (1997) Limitations of temporal resolution in functional MRI. Magn Reson Med 37:631–636
46. Chang C, Thomason ME, Glover GH (2008) Mapping and correction of vascular hemodynamic latency in the BOLD signal. Neuroimage 43:90–102
47. Kruger G, Glover GH (2001) Physiological noise in oxidative-sensitive magnetic resonance imaging. Magn Reson Med 46:631–637
48. Triantafyllou C, Hoge RD, Krueger G, Wiggins CJ, Potthast A, Wiggins GC, Wald LL (2005) Comparison of physiological noise at 1.5 T, 3 T and 7 T, and optimization of fMRI acquisition parameters. Neuroimage 26:243–250
49. Hu X, Le TH, Parish T, Erhard P (1995) Retrospective estimation and correction of physiological fluctuation in Functional MRI. Magn Reson Med 34:201–212
50. Wowk B, McIntyre MC, Saunders JK (1997) K-space detection and correction of physiological artifacts in fMRI. Magn Reson Med 38:1029–1034
51. Biswal B, Deyoe E, Hyde JS (1996) Reduction of physiological fluctuations in fMRI using digital filters. Magn Reson Med 35:107–113
52. Glover GH, Li TQ, Ress D (2000) Image-based method for retrospective correction of physiological motion effects in fMRI: RETROICOR. Magn Reson Med 44:163–167
53. Chuang KH, Chen JH (2001) IMPACT: image-based physiological artifacts estimation and correction technique for functional MRI. Magn Reson Med 46:344–353

54. Le TH, Hu X (1996) Retrospective estimation and correction of physiological artifacts in fMRI by direct extraction of physiological activity from MR data. Magn Reson Med 35:290–298
55. Heinze HJ, Mangun GR, Burchert W, Hinriches H, Scholz M, Munte TF, Gos A, Scherg M, Johannes S, Hundeshagen H, Gazzaniga MS, Hillyard SA (1994) Combined spatial and temporal imaging of brain activity during visual selective attention in humans. Nature 372:543–546
56. Gotman J, Kobayashi E, Bagshaw AP, Bénar C-G, Dubeau F (2006) Combining EEG and fMRI: a multimodal tool for epilepsy research. J Magn Reson Imaging 23:906–920
57. Gonzalez Andino SL, Blanke O, Lantz G, Thut G, GravedePeraltaMenendez R (2001) The use of functional constraints for the neuroelectromagnetic inverse problem: alternatives and caveats. Int J Bioelectromagn 3(1)
58. Arthurs OJ, Boniface SJ (2003) What aspect of the fMRI BOLD signal best reflects the underlying electrophysiology in human somatosensory cortex? Clin Neurophysiol 114:1203–1209
59. Nunez PL, Silberstein RB (2000) On the relationship of synaptic activity to macroscopic measurements: does co-registration of EEG with fMRI make sense? Brain Topogr 13:79–96